L- and M-band annular groove phase mask in lab performance assessment on the vortex optical demonstrator for coronagraphic applications

Aïssa Jolivet,[a,*] Gilles Orban de Xivry,[b] Elsa Huby,[a] Pierre Piron,[c] Ernesto Vargas Catalan,[c] Serge Habraken,[a] Jean Surdej,[a] Mikael Karlsson,[c] and Oliver Absil[a]

[a]Liège University, STAR Institute, bât B5c, Liège, Belgium
[b]CNRS, LESIA, Observatoire de Paris, Université PSL, Sorbonne Université, Université Paris Diderot, Sorbonne Paris Cité, Meudon, France
[c]Uppsala University, Ångström Laboratory, Department of Engineering Sciences, Uppsala, Sweden

Abstract. Coronagraphy is a high-contrast imaging technique that aims to reduce the blinding glare of a star to detect a potential companion in its close environment. Vortex phase mask coronagraphy is widely recognized as one of the most promising approaches. The vortex optical demonstrator for coronagraphic application (VODCA) is a test bench currently developed at the University of Liège. Its main goal is to optically characterize infrared phase masks, in particular vortex masks. We detail the layout and salient features of VODCA and present the performance of the latest L-band (3575 to 4125 nm) and M-band (4600 to 5000 nm) annular groove phase masks (AGPMs) manufactured by our team. We obtain the highest rejection ratio ever measured for an AGPM at L-band: 3.2×10^3 in a narrowband filter (3425 to 3525 nm) and 2.4×10^3 in a broad L-band filter. By providing measurements close to the intrinsic limit of science-grade AGPMs, VODCA proves to be a step forward in terms of the evaluation of vortex phase masks performance. © 2019 Society of Photo-Optical Instrumentation Engineers (SPIE) [DOI: 10.1117/1.JATIS.5.2.025001]

Keywords: infrared test bench; high-contrast imaging; subwavelength grating vortex coronagraph.

Paper 18075 received Sep. 12, 2018; accepted for publication Feb. 19, 2019; published online Apr. 8, 2019.

1 Introduction

The flux ratio (or contrast) between a star and an exoplanet (up to 10^{10} in the case of Earth-like planets) is a great challenge for direct imaging techniques. Coronagraphy provides a means to optically reduce the starlight to enable the detection of very faint objects in its vicinity. Various coronagraphic methods are used for this purpose, based on amplitude or phase masks. Among phase masks, the vortex phase mask[1] is widely recognized as one of the most promising approaches.[2] The vortex phase mask induces a helical phase ramp around its optical axis, which redistributes the light outside the geometric image of the input pupil. A Lyot stop located in a downstream pupil plane prevents the starlight from reaching the detector.

Various implementations of the vortex phase mask are considered in the literature. Here, we focus on a vectorial implementation, where birefringence is induced by etching a subwavelength grating on top of a transparent substrate to produce a spatially variant half-wave plate. The charge-2 vortex phase mask (phase ramp of 4π around the optical axis) based on the subwavelength grating technology is referred to as annular groove phase mask[1,3] (AGPM). The AGPMs presented in this paper have been optimized for achromaticity in the L-band (3.5 to 4.1 μm), a sweet spot for the direct imaging of young planetary systems, where good wavefront quality can be obtained from the ground with standard adaptive optics correction.[3] Other AGPMs have been etched specifically for the H- (1.44 to 1.78 μm), K- (1.95 to 2.35 μm), and N- (11 to 13.2 μm) bands,[4,5] but these are not considered here.

Vortex phase masks are the key elements for large ground-based telescopes to efficiently reduce the stellar glare while keeping a high-throughput and Strehl ratio.[6,7] These phase masks, however, need to be properly qualified before their installation inside the high-contrast imaging instruments. As a part of the VORTEX project, it has become crucial to build and operate our own infrared testing facility at the University of Liège. With the dedicated Vortex Optical Demonstrator for Coronagraphic Application (VODCA) optical test bench,[8] we aim to simulate the coronagraphic procedure as it happens inside a telescope by introducing a light source comparable to a star to assess the quality of the manufactured phase masks. VODCA aims to produce measurements as close as possible to the intrinsic limit of each mask. This limit depends on two factors: the physical dimensions of the mask (sidewall angle, line width, and depth[9]) and the potential defects in the substrate and grating. The AGPM design is based on a rigorous coupled-wave analysis (RCWA[1]). Using realistic parameters, RCWA predicts the best rejection ratio to be >2500 over the L-band with a peak of >3500 at a specific wavelength.[9] Because our applications are essentially ground based, reaching such a high rejection rate is largely sufficient, as the actual on-sky rejection rate will generally be limited to a few hundred by atmospheric turbulence and by the particular shape of the telescope pupil (central obscuration and spider arms).[7] Yet measuring the intrinsic performance of AGPMs is still crucial, because such measurements allow us to derive the exact parameters of the subwavelength grating and thereby evaluate the quality of the manufacturing process.[10]

This paper aims to describe the design (Sec. 2) and operation (Sec. 3) of the VODCA bench and to demonstrate the benefits of

---

*Address all correspondence to Aïssa Jolivet, E-mail: Aissa.Jolivet@uliege.be

using a specially designed coronagraphic bench in the evaluation of phase masks through the updated performance analysis of all L-band AGPMs available to us (Sec. 4). Finally, we discuss the limitations of VODCA in Sec. 5 and conclude in Sec. 6.

2 Vortex Optical Demonstrator for Coronagraphic Applications Test Bench

VODCA is a high-contrast optical test bench (Fig. 1) designed to operate at the same wavelengths as our previously manufactured AGPM,[7–10] i.e., the near- to mid-infrared range corresponding to the H-, K-, L-, and M-bands (between 1.5 and 5 μm). We developed VODCA as a tool to evaluate the AGPM performance using our standard criterion, the null depth or its inverse, the rejection ratio.[3] The rejection ratio is the flux ratio between the coronagraphic (on-axis) point spread function (PSF), obtained with the beam focused at the center of the mask, and the non-coronagraphic (off-axis) PSF, obtained with the beam focused at a sufficiently large distance from the center. In practice, for the latter, we use a decentering of the mask by 2 mm ($>10\lambda/D$) to make sure that the off-axis PSF is not affected by the vortex effect but still take into account the transmission of the mask. We follow the data processing described in Ref. 3, where the flux is integrated over the full width at half-maximum zone of the PSF to compute the rejection ratio. This paper focuses on the evaluation of the L-band AGPM performance. The hardware details that are directly related to this band will be emphasized.

2.1 Hardware

VODCA is divided into two parts. The beam-shaping part detailed in Sec. 2.1.1 includes the sources, the shutter, filters, and neutral densities. Two off-axis parabolas collimate and focus the beam. The second part is dedicated to coronagraphy and is described in Sec. 2.1.2.

2.1.1 Sources and filters

A supercontinuum (SC) laser from Le Verre Fluoré covers a large part of the near- to mid-infrared region we are interested in (1.0 to 4.1 μm). It provides a single-mode fiber output beam for wavelengths above 1.6 μm. The SC laser is always used at

full power as it corresponds to the most stable flux and the broadest spectrum. Owing to source instability, peak-to-valley flux variations can go up to 10%.

For M-band characterization, we use a quantum cascade laser (QCL) from Alpes lasers, which delivers a single-mode narrow-line emission at 4.6 μm. The laser is fiber-coupled, which allows us to use it in place of the SC laser by directly plugging the output fiber to the coronagraphic part of the bench. We typically operate the QCL in a low-flux regime and at a temperature of 25°C. At a constant temperature, this laser source is very stable, with very small flux variations (<1% rms).

We used one broadband and three narrow-band filters (see Table 1) in every astronomical band we cover (H: 1.44 to 1.77 μm, K: 1.95 to 2.35 μm, and L: 3.5 to 4.1 μm). Because the SC laser power decreases at both ends of the spectrum, using narrowband filters in these regions leads to a significantly lower signal-to-noise ratio (SNR) than in the broadband filters. As an extreme example, the SNR with the filter L-BBF (see Table 1) is ~100 times higher than with L-NBF3.

As the source operates at a fixed power and considering the camera dynamic range, neutral densities are needed to avoid saturation of the detector. A shutter is placed after the laser output. This specific position, before the single-mode fiber, guarantees a better background evaluation and subtraction (Sec. 3.1).

It is important to characterize our phase masks over a broadband filter (representative of the L-band) to determine whether they are suitable for integration on ground-based telescopes. Narrowband filters fulfill a different role. The rejection ratio is measured as a function of wavelength and is compared to

Table 1 L-band filters' wavelength characteristics.

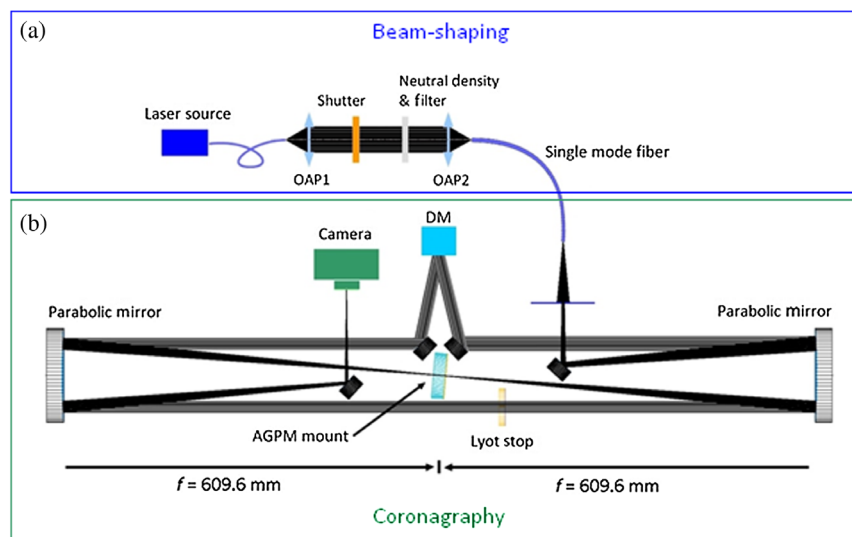| Filter	Wavelength (nm)
L-NBF1	3425–3525
L-NBF2	3710–3890
L-NBF3	3960–4120
L-BBF	3575–4125

Fig. 1 Layout of VODCA, including (a) the beam-shaping part and (b) the coronagraphic part.

RCWA simulations to infer the corresponding grating parameters. This is a crucial step in the characterization of AGPMs, due to the lack of a nondestructive metrological method for the measurement of the grating depth.[9] The optical evaluation is thus necessary to determine whether the grooves have been etched too deep or too shallow, which can subsequently be improved by an additional etching step. Re-etching has been done successfully on several components, and it has significantly improved their rejection ratio.[9]

2.1.2 Optical design and camera

We designed a fully reflective bench to avoid chromatic aberrations. Two parabolas ($f = 609.6$ mm) and flat mirrors are used to collimate, focus, and direct the beam. The AGPM is placed at the focal point, common to both parabolas. An ALPAO deformable mirror (DM) with 97 actuators is used to correct for low-order static aberrations on the bench. The size of the collimated beam and of the circular pupil is defined by the DM itself ($\varnothing = 13.5$ mm). The f-number ($f\#$) on the phase mask is $f/45$. The AGPM is set on a rotation stage combined with a three-axis Newport mount with piezo actuators, which accurately produces 10-nm steps. The light diffracted outside the geometric pupil by the phase mask is blocked by a Lyot stop, with a size reduced to 80% of the pupil (10.8 mm), placed in a downstream pupil plane. The beam is then focused and imaged onto the 512×640 pixels of our infrared camera (FLIR Systems, A6700sc) cooled down to 77 K. Assuming 3.6 and 4.1 μm as extreme values for the wavelengths (λ) allowed by our broad L-band filter, the PSF core size varies between 167 and 190 μm on the AGPM. On the camera (15-μm pixel pitch), the PSF core is sampled with a number of pixels ranging from 14 to 16.

2.2 Software

2.2.1 LabVIEW interface

The hardware of VODCA, including the camera, the shutter, and the three-axis motorized piezoactuator mount of the AGPM, are controlled by the same LabVIEW interface designed specifically for this optical bench. It includes a routine to automatically align the AGPM center on the core of the PSF with extremely good accuracy and repeatability (see Sec. 3.3).

2.2.2 Python interface and aberrations minimization routine

A dedicated python interface has been developed for the DM control. As mentioned earlier, VODCA features a 97-actuator DM that provides additional leverage in terms of aberration control on the bench. The software allows fast operations and online monitoring of the performance. We implement a simple and empirical technique to optimize the postcoronagraphic light rejection inspired from image-sharpening techniques. Details can be found in Ref. 11, and we summarize hereafter our procedure based on the analysis of postcoronagraphic PSFs:

1. Selection of a metric and of a minimization algorithm.

2. Selection of a modal basis (e.g., Zernike or mirror modes), the coefficients of which are the free parameters of the optimization problem.

3. For each iteration, acquisition of a number of frames, evaluation of the metric, and computation of the next solution on the modal basis.

This PSF-sharpening technique for coronagraphy has brought some noticeable gain on the measured peak rejection ratio by improving the wavefront control and the repeatability of the measurements. It is, however, expensive in terms of data frame requirement and is thus quite time-consuming. Detailed limitations and performance are discussed in Ref. 11, and the aspect of wavefront stability delivered by the DM is further discussed in Sec. 3.2. Minimizing the wavefront aberrations is a necessary prerequisite before starting the AGPM evaluation.

3 Test Protocol

3.1 Background Subtraction

The shutter used for the background subtraction is synchronized with the camera through the LabVIEW interface, to obtain background measurements and subtract them from the scientific frames in real time. Every frame acquisition is thus systematically followed by an acquisition of a background frame. One single background measurement for a whole sequence of acquisitions has proved to be insufficient to capture background fluctuations. For each off- and on-axis datum, we average 100 individual background-subtracted frames.

3.2 Aberrations Correction Stability

Before actually recording the science frames on VODCA, the first step is to ensure that the wavefront is as flat as possible. To do so, we use the procedure described in Sec. 2.2.2 and correct up to 97 modes with the DM. Because the low flux in the wings of the attenuated PSF can make high-order corrections inaccurate, it is common to set 90 as an upper limit for the number of corrected modes.

The mirror and the bench as a whole are subject to slow mechanical drifts with time. When the DM correction is no longer up to date, the wavefront quality will eventually decrease below a satisfactory level. As a consequence, the measured rejection ratio will decrease with time, as shown in Fig. 2. Setting a maximal variation of the rejection ratio measurements to 5%, we conclude that all the measurements with a given mask have to be taken within 2 h after the minimization of the aberrations. In the vast majority of cases, measurements on the same mask are performed within a shorter timespan (typically <30 min).
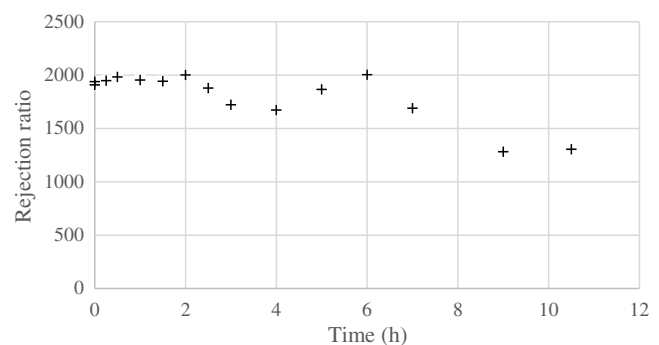

Fig. 2 Rejection ratio measurements as a function of time with the same DM correction.

3.3 Centering Routine

Due to the vortex coronagraph being very sensitive to pointing (i.e., tip-tilt errors), it is crucial to ensure that the phase mask is properly aligned with respect to the beam. Any deviation from this optimal position will result in an additional, unwanted leakage affecting the measured performance.

Manual positioning is a great source of uncertainty in the early performance assessment. Several alignment trials are required to minimize the pointing-induced leakage, introducing a non-negligible source of variability in the measurements. An automatic routine has been designed to fix this. Our minimization criterion is the total flux in the PSF core. This routine is less time-consuming and the centering achieved is more precise and reproducible. The protocol is a four-step process, using scans along the x and y axes with two different steps (large, 1 μm; and small, 0.25 μm) to find the optimal position. We first use a basic quadratic model[12] of the leakage to infer the vortex position based on a large-step grid, and then use smaller, incremental steps around the calculated minimum for an improved accuracy.
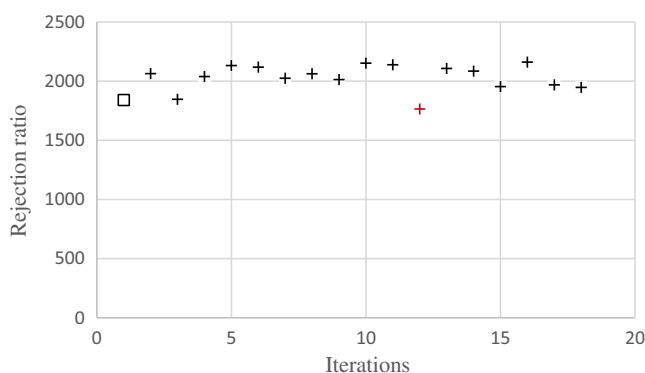

Fig. 3 Rejection ratio obtained after 17 successive runs of the centering routine. The square shows the rejection ratio measured just after the minimization of the aberration on the DM. The red cross is a failed attempt (optimal position meeting the criteria is not found) of the routine to successfully find the optimal position.

Given the hysteresis inherent to the actuators, relying only on the calculated fit of the data leads to unacceptable errors on the positioning. A balance has to be found between the accuracy, the robustness, and the duration of the centering procedure. Accuracy and robustness are affected by turbulence, vibrations, and source fluctuations, whereas the bench stability limits the duration (Sec. 3.2). The most accurate routine (capability of finding the best position) would imply a low robustness (rate of success for achieving the accuracy criterion) and/or an unacceptable duration (>15 min).

The standard parameters for the centering routine lead to an optimization duration of <5 min while providing a sufficiently high accuracy and robustness for our purpose. For example, repeating the centering procedure 17 times on a high-quality AGPM provides a mean rejection rate of 2023 with a standard deviation of 116 (5.7%) and a success rate of 94% (see Fig. 3).

4 Annular Groove Phase Mask Test Results (L-band)

In this section, we report the performance measured for a series of L-band AGPMs manufactured at the Uppsala University, Sweden, in the past 5 years (see Table 2). All measurements are obtained after minimizing the aberrations with the procedure outlined in Sec. 2.2.2 and centering the beam on the AGPM, as discussed in Sec. 3.3.

4.1 Rejection Ratio Measurements

The L-band AGPMs were tested in the L-band with the SC source in the broadband and narrowband filters, as well as in the M-band using the 4.6-μm laser source, to check if they meet the requirements for scientific operation with a ground-based 10-m class telescope. The results have been compiled in Table 3, where AGPMs identified with a "r" have been re-etched to improve their original coronagraphic performance. The re-etching consisted mostly in tuning the etch depth.[10] In the case of AGPM-L9r2, this procedure was done twice. The quoted error bars were representative of the variability in the rejection

Table 2 Best AGPM rejection ratio measured on VODCA with L-band filters (Table 1) and in the M-band (monochromatic source). The accuracy of the centering routine (± 1-σ, Sec. 3.3) defines the errors on the rejection ratio.

	Rejection Ratio				
AGPM	L-BBF	L-NBF1	L-NBF2	L-NBF3	4.6 μm
AGPM-L4	566 ± 32	292 ± 17	669 ± 38	789 ± 45	70 ± 4
AGPM-L5	1501 ± 86	588 ± 34	2092 ± 119	1715 ± 98	48 ± 3
AGPM-L8	168 ± 10	94 ± 5	64 ± 4	32 ± 2	18 ± 1
AGPM-L9r2	852 ± 49	337 ± 19	924 ± 53	830 ± 47	141 ± 8
AGPM-L11r	2404 ± 137	3213 ± 183	1683 ± 96	543 ± 31	75 ± 4
AGPM-L12r	84 ± 5	86 ± 5	87 ± 5	146 ± 8	1773 ± 95
AGPM-L13r	176 ± 10	92 ± 5	207 ± 12	483 ± 28	134 ± 7
AGPM-L14	864 ± 49	258 ± 15	995 ± 57	802 ± 46	55 ± 3
AGPM-L15	1430 ± 82	717 ± 41	1378 ± 79	1448 ± 83	50 ± 3

Table 3 Comparison between the best results with the L-BBF filter on VODCA and YACADIRE.

AGPM	VODCA (with DM)	VODCA (without DM)	YACADIRE
AGPM-L4[a]	566 ± 32		500 ± 75
AGPM-L5	1501 ± 86	950 ± 54	620 ± 93
AGPM-L8	168 ± 10	52 ± 3	60 ± 9
AGPM-L9r2	852 ± 49	536 ± 31	397 ± 60
AGPM-L11r	2404 ± 137	1300 ± 74	984 ± 148
AGPM-L14[a]	864 ± 49		370 ± 56
AGPM-L15	1430 ± 82	1251 ± 71	628 ± 94

[a]Note: AGPM L4 and L14 have not been tested without DM due to their limited availability.

ratio measurements, which were repeated several times for each AGPM.

4.2 Comparison with YACADIRE

Characterizing the same AGPMs on different benches provides a tool to evaluate the optical quality of the bench. Some AGPMs have been tested in the past on the YACADIRE[3] test bench at the Paris Observatory. The rejection ratios measured with this bench are globally lower than those measured on VODCA (see Table 4). The protocol for data acquisition is the same; however, neither automated centering routine nor DM is available on YACADIRE. Reducing aberrations through better alignment and better wavefront correction is the key to reach the intrinsic limit of the AGPMs in terms of rejection ratio. Other factors such as SNR and accurate mask-centering had been also taken into account while designing and building VODCA. It confirms

Table 4 AGPM transmission in the L-BBF filter and at 4.6 μm. Error bars are included only for AGPMs that have been measured several times. AGPM-L13 has not been evaluated in the L-band due to its limited availability.

	Transmission	
AGPM	L-BBF	4.6 μm
AGPM-L4	82%	66%
AGPM-L5	85.4% ± 0.1	61%
AGPM-L8	82.9% ± 0.4	62%
AGPM-L9r2	84.7% ± 0.9	70% ± 3
AGPM-L11r	83.7% ± 0.1	58% ± 2
AGPM-L12r	85% ± 0.7	68.5% ± 2.5
AGPM-L13[a]		64%
AGPM-L14	83%	65%
AGPM-L15	83.5% ± 0.5	66% ± 1

the overall better optical quality of VODCA. Unfortunately, no in-depth study has been performed to evaluate with precision the error budget of the measured rejection ratios on YACADIRE. The masks have been measured repeatedly and the dispersion of the measurements has led us to estimate typical statistical errors to be around 15%. To provide a fairer comparison between the VODCA and the YACADIRE results, we also quote the rejection ratios measured on VODCA without wavefront control. The quality of these measurements is reduced compared to the case with wavefront control, as discussed below (Sec. 5.1), but it is still significantly higher than on YACADIRE, owing to the more optimal design and to the automatic centering procedure.

4.3 Transmission Measurements

Each AGPM has an antireflective grating (ARG) etched on the backside of its diamond substrate to reduce internal reflections inside the phase mask.[10] As a consequence, the rejection ratio is improved as well as the transmission of the AGPM. The bare diamond substrate has a ~17% backside reflection in the L-band, reduced to ~1.9% thanks to the ARG.[3] The theoretical transmission in the L-band is expected to be ~87% (limited by phonon absorption in the diamond substrate).

Using the L-BBF filter, an off-axis PSF image is compared to a reference image without the phase mask in the optical train, to compute the transmission of the AGPM. The same procedure is repeated with the 4.6-μm laser source. The transmission is presented in Table 5. All AGPMs show a transmission in the 82% to 85% range at L-band, close to our expectations. The measured transmission significantly decreases in the M-band, due to increased phonon absorption around 4.6 μm.

5 Vortex Optical Demonstrator for Coronagraphic Applications Optical Quality and Limitations

5.1 Influence of Wavefront Correction

In the case of broadband measurements, an AGPM will never produce a perfect cancellation of the starlight due to chromatic errors in the π phase shift induced between the two orthogonal polarizations by the subwavelength grating. The textbook effect of chromatic errors is to produce a scaled-down version of the non-coronagraphic PSF.[1] This is illustrated in Fig. 4, where the VODCA bench is operated without DM, using one of the available AGPM (AGPM-L11r). The coronagraphic PSF is slightly broadened compared to the off-axis PSF, but it corresponds

Table 5 Simulation parameters.

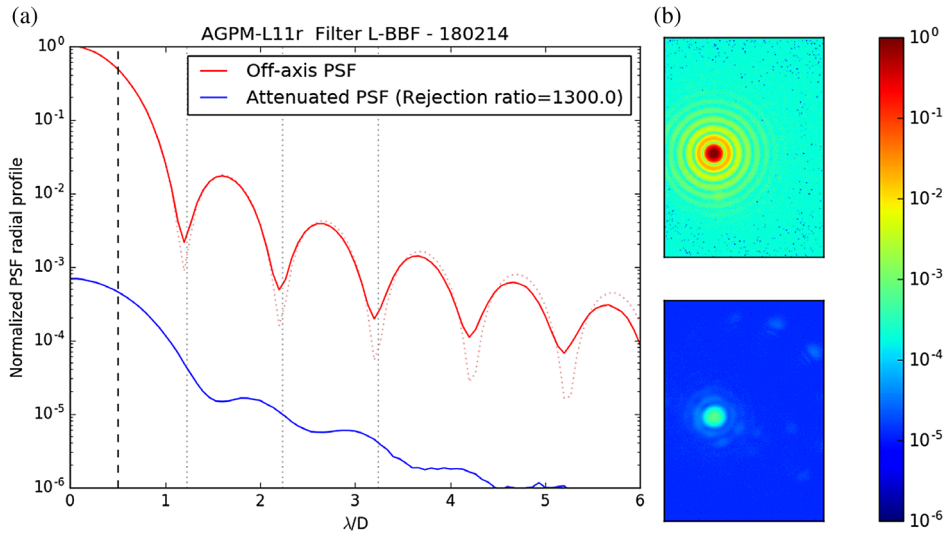|	
Fraction Lyot stop	80%
Central obscuration	None
Intrinsic rejection ratio	2404
Wavelength (μm)	3.75
Number of Zernike modes	100
Number of images averaged before radial profile	100
Wavefront error rms (nm)	30

(a)

(b)

Fig. 4 (a) Radial profiles of the coronagraphic (blue) and noncoronagraphic (red) PSFs, using the same undersized Lyot stop. The dashed vertical line represents the area over which the flux is integrated to calculate the rejection ratio. The dashed red lines correspond to the theoretical Airy pattern. (b) Illustration of the off-axis (top) and on-axis (bottom) PSFs.

otherwise rather well to the expected, scaled-down version of the off-axis PSF. The broadening of the central part of the PSF points toward the presence of low-order aberrations, whereas very little high-order aberrations seem to affect the contrast curve at larger separations.

The same measurements are then repeated after inserting the DM in the optical train and optimizing its shape to minimize the rejection ratio, as described in Sec. 2.2.2. In Fig. 5 the same measurements (same AGPM) as Fig. 4 are displayed, with aberrations control by the DM. Two main differences can be noted with respect to Fig. 4: a higher rejection ratio (2400 instead of 1300) and a higher starlight level beyond $1 \lambda/D$. The higher rejection ratio suggests that the intrinsic limit of the AGPM in terms of starlight rejection is not reached in the first measurement without DM while the increased residuals at larger separation point toward increased aberrations at the corresponding

spatial frequencies. It introduces noncorrected speckles responsible for the plateau shape of the attenuated PSF noticeable after $1.5 \lambda/D$. Considering the 97 actuators of the DM, it should correct up to $5 \lambda/D$[11].

This behavior can be reproduced through simulations, as illustrated in Fig. 6. Though the DM should in principle reduce the level of aberrations for all spatial frequencies up to $5 \lambda/D$, this correction is only designed to minimize a figure of merit and therefore does not necessarily provide the best wavefront quality. We have simulated the influence of wavefront errors, evenly distributed between the first 100 Zernike modes, as described in Table 2. The plateau observed at a level of about 4×10^{-4} in the coronagraphic PSF can then be reproduced with a total wavefront error of 30-nm rms, which means an rms error of 3 nm for each individual Zernike mode. The level of the plateau is roughly proportional to rms error on each mode, whereas the
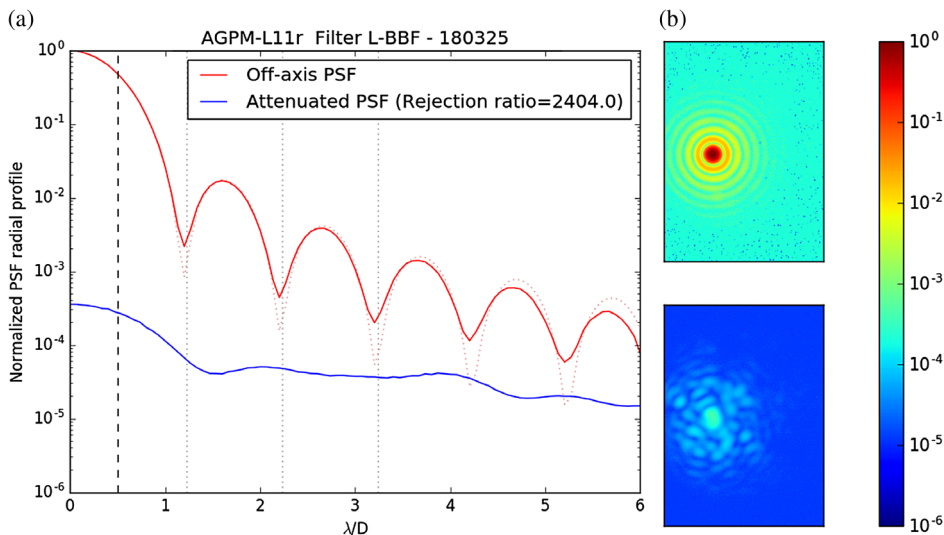
(a)

(b)

Fig. 5 Left: Example of the comparison of the normalized radial fluxes centered on the PSF between an off-axis (red) and an attenuated PSF (blue, AGPM on-axis). The dashed vertical line represents the area over which the flux has been integrated to calculate the rejection ratio. The dashed red lines close to the off-axis PSF correspond to the theoretical Airy pattern of minima.
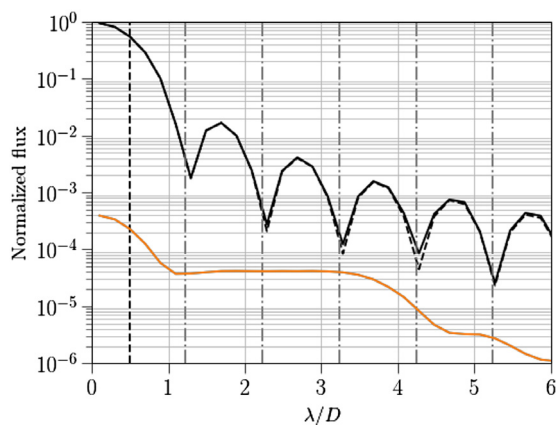
Fig. 6 Simulated off-axis (black) and coronagraphic (orange) PSFs using the parameters of Table 2.

Fig. 7 Theoretical rejection ratio computed as a function of the amplitude of five low-order aberrations (Z2: tip, Z4: focus, Z5: astigmatism, Z6: coma, and Z7: trefoil).

spatial extent of the plateau depends on the number of modes included.

For these measurements and simulations, we conclude that using wavefront control (as described in Sec. 2.2.2) not only significantly reduces the power in the lowest aberration orders but also increases the aberration level in higher-order modes within the DM control region, and thereby reduces performance beyond about $1\,\lambda/D$. Without DM, the bench presents a higher level of low-order aberrations (i.e., lower attenuation on the PSF core) but lower high-order aberrations, as the radial profile intensity decreases as expected with angular separation (as in aberration-free simulations). We note that the estimated level of aberrations in the presence of the DM (30-nm rms spread onto 100 modes) is significantly larger than the expected best flat for the DM (=12.22-nm rms measured by the manufacturer). This suggests that a better correction would be possible by implementing a better wavefront control strategy, based, e.g., on a bona fide infrared wavefront sensor.

5.2 *Optical Quality*

Vibrations and turbulence are expected to affect the rejection ratios measured on VODCA. To evaluate their influence, we measure the motion of the noncoronagraphic PSF onto the detector. A peak-to-valley motion of $\sim$0.4 pixel ($=6\,\mu$m) is measured, which corresponds to about $0.035\,\lambda/D$ at L-band. Assuming that the same level of vibration affects the beam at the intermediate focus where the AGPM is located (a pessimistic assumption as the detector is the main source of vibration on the bench), this would lead to an additional stellar leakage of only about 2×10^{-4}, which is negligible compared to the intrinsic performance of the AGPMs to be tested.

Beyond pointing jitter, charge-2 vortex phase masks like the AGPM are known to be sensitive to low-order aberrations in general.[13] Simulations of a perfect AGPM in L-band with an 80% Lyot stop (as VODCA) and no central obstruction have been carried out to estimate the maximum aberration level that can be tolerated in order to measure rejection ratios $>10^3$. The analysis is performed independently for the main low-order Zernike modes Z2 (tip), Z4 (focus), Z5 (astigmatism), Z7 (coma), and Z9 (trefoil). For each of these modes, we have varied the wavefront rms and simulated off- and on-axis PSFs. For each couple of PSFs, we have computed the rejection ratio. The results are illustrated in Fig. 7. The aberration level where the
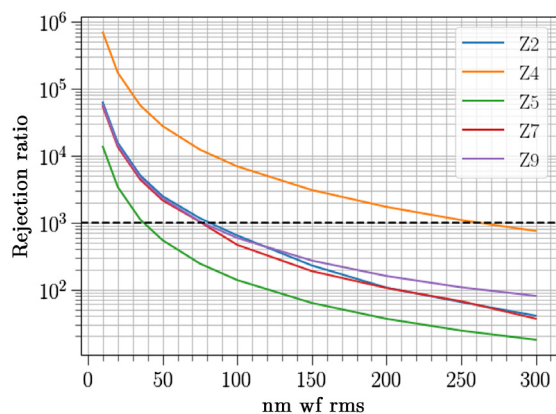
Table 6 Aberrations level limiting the rejection ratio (RR) to 10^3 and 2×10^3.

	Wavefront rms (nm)	
Mode	RR $= 10^3$	RR $= 2 \times 10^3$
Z2	81	26
Z4	260	84
Z5	37	12
Z7	76	24
Z9	76	25

rejection ratio reaches 10^3 (resp. 2×10^3) is listed for each mode in Table 6.

Our simulations show that the rejection ratio is particularly sensitive to astigmatism while quite resilient to focus. This is because the additional stellar leakage induced by focus errors mostly affects the first Airy ring. The rejection ratio, which is computed on the PSF core, is therefore not as affected as for the other aberrations, but the performance still significantly decreases in the first Airy ring and beyond.

As a rejection ratio of around 2400 (resp. 3200) is obtained in broadband (resp. narrowband) for the best AGPM (AGPM-L11r), we conclude that the aberrations in the lower order modes are not larger than the values given in the right-most column of Table 6. Actually, because this analysis pertains to each mode taken separately, the aberrations are probably much smaller than these limits and probably of the order of 3 nm rms per mode, as discussed in Sec. 5.1. The VODCA bench is probably capable of measuring rejection ratios even >3000, although it is hard to evaluate the exact bench limitation in the absence of an actual infrared wavefront sensor.

6 Conclusions

The high-contrast coronagraphic test bench VODCA was presented. The optical layout and procedure for evaluating the quality of our AGPM was described in detail. With VODCA, we achieved the highest rejection ratios ever measured for

AGPMs at L-band. We were able to reach a rejection ratio as high as 3.2×10^3 in a narrowband filter (3425 to 3525 nm) and as high as 2.4×10^3 in the broad L-band (3575 to 4125 nm) for AGPM-L11r. These rejection ratios were consistent with the intrinsic, chromatic limits of AGPMs based on RWCA simulations.[10] They proved that (i) our etching techniques have reached a sufficient accuracy to produce AGPMs with the highest possible performance and (ii) that the VODCA bench provides a sufficiently high optical quality to measure the intrinsic limit of any foreseeable AGPM. In addition, VODCA provides an essential tool to accurately assess the AGPM grating parameters by combining accurate measurements in several narrowband filters with RCWA modeling. This new feature, coupled with a continuously improving manufacturing process has led to the successful re-etching of AGPM to improve their performance[9] (up to the theoretical limit set by chromatism in the whole L-band).

Operating with high-performance phase masks highlights the major role played by wavefront quality. We showed that the contrast measured for separation $>1\,\lambda/D$ depended critically on the aberration distribution on the bench. This distribution is mostly affected by the surface control and the quality of the DM.

In future, VODCA will be used to test various apodization solutions for actual telescope pupils and to explore novel focal-plane wavefront-sensing techniques.

Acknowledgments

References

1. D. Mawet et al., "Annular groove phase mask coronagraph," *Astrophys. J.* **633**, 1191–1200 (2005).
2. O. Guyon et al., "Theoretical limits on extrasolar terrestrial planet detection with coronagraphs," *Astrophys. J. Suppl. Ser.* **167**, 81–99 (2006).
3. C. Delacroix et al., "Laboratory demonstration of a mid-infrared AGPM vector vortex coronagraph," *Astron. Astrophys.* **553**, A98 (2013).
4. C. Delacroix et al., "A diamond AGPM coronagraph for VISIR," *Proc. SPIE* **8446**, 84468K (2012).
5. E. Vargas Catalan et al., "Subwavelength diamond gratings for vortex coronagraphy: towards annular groove phase mask for shorter wavelengths and topological charge 4 designs," *Opt. Mater. Express* **8**(7), 1976–1987 (2018).
6. O. Absil et al., "The VORTEX project: first results and perspectives," *Proc. SPIE* **9148**, 91480M (2014).
7. O. Absil et al., "Three years of harvest with the vector vortex coronagraph in the thermal infrared," *Proc. SPIE* **9908**, 99080Q (2016).
8. A. Jolivet et al., "The VORTEX coronagraphic test bench," *Proc. SPIE* **9151**, 91515P (2014).
9. P. Forsberg and M. Karlsson, "High aspect ratio optical gratings in diamond," *Diamond Relat. Mater.* **34**, 19–24 (2013).
10. E. V. Catalan et al., "Optimizing the subwavelength grating of L-band annular groove phase masks for high coronagraphic performance," *Astron. Astrophys.* **595**(A127), 1–8 (2016).
11. G. O. de Xivry et al., "Post-coronagraphic PSF sharpening with the vortex coronagraph," in *Conf. Adapt. Opti. for Extremely Large Telescopes 5* (2017).
12. E. Huby et al., "Post-coronagraphic tip-tilt sensing for vortex phase masks: the QACITS technique," *Astron. Astrophys.* **584**(A74), 12 (2015).
13. D. Mawet et al., "The vector vortex coronagraph: sensitivity to central obscuration, low-order aberrations, chromaticism, and polarization," *Proc. SPIE* **7739**, 773914 (2010).

Biographies of the authors are not available.